Monthly Notices of the ROYAL ASTRONOMICAL SOCIETY

MNRAS **498,** 4192–4204 (2020)
Advance Access publication 2020 August 22

doi:10.1093/mnras/staa2545

ALMA characterizes the dust temperature of $z \sim 5.5$ star-forming galaxies

Andreas L. Faisst [1]★ Yoshinobu Fudamoto [2]★ Pascal A. Oesch [2,3] Nick Scoville [4] Dominik A. Riechers [5,6] Riccardo Pavesi [5] and Peter Capak [3,4]

[1]*IPAC, California Institute of Technology 1200 E California Boulevard, Pasadena, CA 91125, USA*
[2]*Observatoire de Genève, Université de Genève, 51 Ch. des Maillettes, CH-1290 Versoix, Switzerland*
[3]*Cosmic Dawn Center (DAWN) at the Niels Bohr Institute, University of Copenhagen and National Space Institute, Technical University of Denmark, 2100 Copenhagen, Denmark*
[4]*California Institute of Technology, MC 249-17, 1200 East California Boulevard, Pasadena, CA 91125, USA*
[5]*Department of Astronomy, Cornell University, Space Sciences Building, Ithaca, NY 14853, USA*
[6]*Max-Planck-Institut für Astronomie, Königstuhl 17, D-69117 Heidelberg, Germany*

Accepted 2020 August 9. Received 2020 July 18; in original form 2020 May 12

ABSTRACT

The infrared (IR) spectral energy distributions (SEDs) of main-sequence galaxies in the early Universe ($z > 4$) is currently unconstrained as IR continuum observations are time-consuming and not feasible for large samples. We present Atacama Large Millimetre Array Band 8 observations of four main-sequence galaxies at $z \sim 5.5$ to study their IR SED shape in detail. Our continuum data (rest-frame 110 μm, close to the peak of IR emission) allows us to constrain luminosity-weighted dust temperatures and total IR luminosities. With data at longer wavelengths, we measure for the first time the emissivity index at these redshifts to provide more robust estimates of molecular gas masses based on dust continuum. The Band 8 observations of three out of four galaxies can only be reconciled with optically thin emission redward of rest-frame 100 μm. The derived dust peak temperatures at $z \sim 5.5$ (30–43 K) are elevated compared to average local galaxies, however, ~ 10 K below what would be predicted from an extrapolation of the trend at $z < 4$. This behaviour can be explained by decreasing dust abundance (or density) towards high redshifts, which would cause the IR SED at the peak to be more optically thin, making hot dust more visible to the external observer. From the 850-μm dust continuum, we derive molecular gas masses between 10^{10} and 10^{11} $M_\odot$ and gas fractions (gas over total mass) of 30–80 per cent (gas depletion times of 100–220 Myr). All in all, our results provide a first measured benchmark SED to interpret future millimetre observations of normal, main-sequence galaxies in the early Universe.

Key words: dust, extinction – galaxies: high-redshift – galaxies: ISM.

1 INTRODUCTION

Galaxies evolve significantly during the first 1–2 Gyr after the big bang. Specifically, after the Epoch of Reioinization at redshifts $4 < z < 6$, galaxies establish fundamental properties as they transition from a primordial to a more mature state. For example, altered optical line ratios are consistent with a harder ionizing radiation field in early galaxies and/or a changing configuration of molecular clouds from density to radiation bounded (e.g. Labbé et al. 2013; de Barros, Schaerer & Stark 2014; Nakajima & Ouchi 2014; Faisst 2016; Harikane et al. 2019). Connected to this, the average metal content of galaxies is increasing from sub-solar to solar during this time (Ando et al. 2007; Mannucci et al. 2010; Faisst et al. 2016b). Going along with the metal enrichment is the rapid growth in stellar mass through mergers and the accretion of pristine gas (Bouché et al. 2012; Lilly et al. 2013; Faisst et al. 2016a; Davidzon et al. 2017; Scoville et al. 2017; Davidzon et al. 2018). Finally, the ultraviolet (UV) colours of galaxies at high redshifts tend to be bluer compared to their descendants, which is indicative of less reddening of their UV light due to dust (e.g. Bouwens et al. 2009, 2012; Finkelstein et al. 2012).

The Atacama Large (Sub-) Millimetre Array (ALMA) has enabled us to extend these previous studies into the far-infrared (far-IR) light through observations of the far-IR continuum and emission lines, commonly the singly ionized Carbon atom (C^+, 158 μm), in normal main-sequence galaxies at >4 (e.g. Walter et al. 2012; Riechers et al. 2014; Capak et al. 2015; Willott et al. 2015). The recently completed *ALMA Large Program to Investigate C^+ at Early Times* (*ALPINE*, Le Fèvre et al. 2019; Bethermin et al. 2020; Faisst et al. 2020)[1] provides such measurements for the largest sample of $z = 4-6$ main-sequence galaxies to-date. *ALPINE* builds the state-of-the-art for the characterization of dust and gas in early galaxies in conjunction with the wealth of ancillary UV and optical data sets (see also Faisst et al. 2019).

From these ALMA observations, our understanding of the interstellar medium (ISM) of galaxies in the early Universe has strongly progressed. The evolution of the IRX−β relation[2] with redshift has

★ E-mail: afaisst@caltech.edu (ALF); Yoshinobu.Fudamoto@unige.ch (YF)

[1]http://alpine.ipac.caltech.edu
[2]It relates the ratio of rest-UV and total IR luminosity to the rest-UV continuum slope β (Meurer, Heckman & Calzetti 1999).

Table 1. Summary of observations.

ID	Band 6			Band 7			Band 8		
	PID	Resolution	σ (μJy)	PID	Resolution	σ (μJy)	PID	Resolution	σ (μJy)
HZ4	2015.1.00388.S[a]	1.1 arcsec	14	2017.1.00428.L[c]	0.93 arcsec	21	2018.1.00348.S[e]	0.71 arcsec	34
HZ6	2015.1.00388.S[a], 2015.1.00928.S[b]	1.4 arcsec	23	2017.1.00428.L[c]	0.89 arcsec	29	2018.1.00348.S[e]	0.73 arcsec	40
HZ9	2015.1.00388.S[a]	1.4 arcsec	14	2012.1.00523.S[d]	0.58 arcsec	41	2018.1.00348.S[e]	0.73 arcsec	57
HZ10	2015.1.00388.S[a], 2015.1.00928.S[b]	1.2 arcsec	21	2012.1.00523.S[d]	0.58 arcsec	53	2018.1.00348.S[e]	0.68 arcsec	66

Notes. The quoted σ represents the RMS of the continuum images per beam. [a]Lu et al. (2018), [b]Pavesi et al. (2019), [c]Bethermin et al. (2020), [d]Capak et al. (2015), and [e]this work.

taught us about changes in dust attenuation. While most galaxies at $z < 4$ show similar dust attenuation properties as local starburst galaxies (e.g. Fudamoto et al. 2017), recent studies based on the *ALPINE* sample suggest a significant drop in dust attenuation at $z > 4$ (Fudamoto et al. 2020) thereby approaching the dust properties of the metal-poor Small Magellanic Cloud (Prevot et al. 1984). Furthermore, the total IR luminosity is crucial to derive total star formation rates (SFRs, Kennicutt 1998) that tell about the true growth rates of galaxies at high redshifts and the evolution of the main-sequence with cosmic time (Khusanova et al. 2020). Finally, the far-IR dust continuum emitted in the optically thin Rayleigh–Jeans (RJ) part of the far-IR spectral energy distribution (SED) at > 250 μm has turned out to be a good proxy of the total molecular gas mass of a galaxy (e.g. Scoville et al. 2014). This alternative method is crucial as deriving gas masses directly from observations of CO transitions is time-consuming at these redshifts. Studies of large samples of galaxies with far-IR continuum measurements up to $z \sim 6$ provide important constraints on the evolution of molecular gas and help us to understand how these galaxies form (Scoville et al. 2016; Kaasinen et al. 2019; Dessauges-Zavadsky et al. 2020).

However, the robustness of the results mentioned above is significantly limited by the fact that the IR SED is inherently unknown at high redshifts (see Faisst et al. 2017). The relative faintness of these galaxies makes IR continuum measurements time-consuming and they are often secondary and only pursued in parallel with the observation of strong far-IR emission lines such as C^+, [N II], or [O III]. The measurement of all IR quantities (total luminosities, SFRs, molecular gas masses, etc.) are therefore significantly relying on assumptions on the shape of the IR SED. These assumptions are commonly based on SEDs of galaxies at lower redshifts. The luminosity weighted temperature of the IR SED is one of the key variables that define its shape. As shown in Faisst et al. (2017), using an average temperature based on low-redshift galaxies can underestimate the true total IR luminosity by up to a factor of 5. There is observational and theoretical evidence that galaxies at high redshifts are warmer (e.g. Magdis et al. 2012; Magnelli et al. 2014; Béthermin et al. 2015; Ferrara et al. 2017; Schreiber et al. 2018; Liang et al. 2019; Ma et al. 2019; Sommovigo et al. 2020), which could be related to their lower metal content or higher star formation density. Such a relation is expected from studies of local galaxies (Faisst et al. 2017). To characterize changes in the IR SED of galaxies at $z > 4$ to verify (or disprove) current assumptions, wavelengths closer to the peak of the IR emission (around rest-frame 100 μm) have to be probed.

In this paper, we present new ALMA measurements at rest-frame 110 μm (Band 8) for four main-sequence galaxies at $z \sim 5.5$. Note that Band 8 provides the strongest constraints on the location of the peak of the IR SED (and hence luminosity weighted dust temperature) while minimizing the observation time with ALMA. These measurements are combined with archival data at rest-frame 150 (Band 7) and 205 μm (Band 6) to provide improved constraints on the IR SEDs of high-redshift galaxies. A comparison to lower redshifts gives us important insights into the evolution of dust properties.

This paper is organized as follows: In Section 2, we detail our new observations together with the archival data. In Section 3, we outline the procedure of fitting the IR SEDs together with the measurements of dust temperature, total IR luminosities, and molecular gas masses. We discuss the temperature−redshift evolution and a possible physical meaning using an analytical model in Section 4 and conclude in Section 5. Throughout this work, we assume a Lambda cold dark matter cosmology with $H_0 = 70\,\mathrm{km\,s^{-1}\,Mpc^{-1}}$, $\Omega_\Lambda = 0.70$, and $\Omega_\mathrm{m} = 0.30$. All magnitudes are given in the AB system (Oke 1974) and stellar masses and SFRs are normalized to a Chabrier (2003) initial mass function (IMF).

2 DATA

We focus on four main-sequence galaxies to which we refer to as *HZ4* ($z = 5.544$), *HZ6* ($z = 5.293$),[3] *HZ9* ($z = 5.541$), and *HZ10* ($z = 5.657$) in the following. These galaxies have been previously discussed by Riechers et al. (2014) and Capak et al. (2015) and are initially spectroscopically selected via Lyα and UV absorption lines from a large spectroscopic campaign with Keck/DEIMOS (Hasinger et al. 2018) on the Cosmic Evolution Survey (COSMOS, Scoville et al. 2007) field. All galaxies have been observed with different ALMA programmes covering their rest-frame wavelengths from 100 to 200 μm (see Table 1).

2.1 New ALMA Band 8 observation

All four galaxies have been observed recently as part of the ALMA programme #2018.1.00348.S (PI: Faisst) at a frequency of 406.4 GHz (Band 8). This frequency was chosen to optimize the constraints on the IR SED and to minimize the integration time to reach a signal-to-noise ratio (S/N) of 10. At that frequency, the Band 8 atmospheric transmission is maximized and going to higher frequencies would increase the integration times significantly. On the other hand, Band 7 observes too low frequencies for robust constraints on the IR SED together with the archival ALMA observations (see appendix in Faisst et al. 2017). In the rest frame of *HZ4*, *HZ6*, *HZ9*, and *HZ10*, Band 8 corresponds to wavelengths of 112.8, 117.3, 112.9, and 111.0 μm, respectively. The observations were carried out in Cycle 6 between 2019 January 9 and 12 in the C43-2 compact configuration (maximal baseline ~ 300 m) at an angular resolution of 0.55 to 0.62 arcsec under good weather conditions (precipitable water vapour column between 0.38 and 0.87 mm). The on-source exposure

[3]This galaxy is also known as *LBG-1* in Riechers et al. (2014).

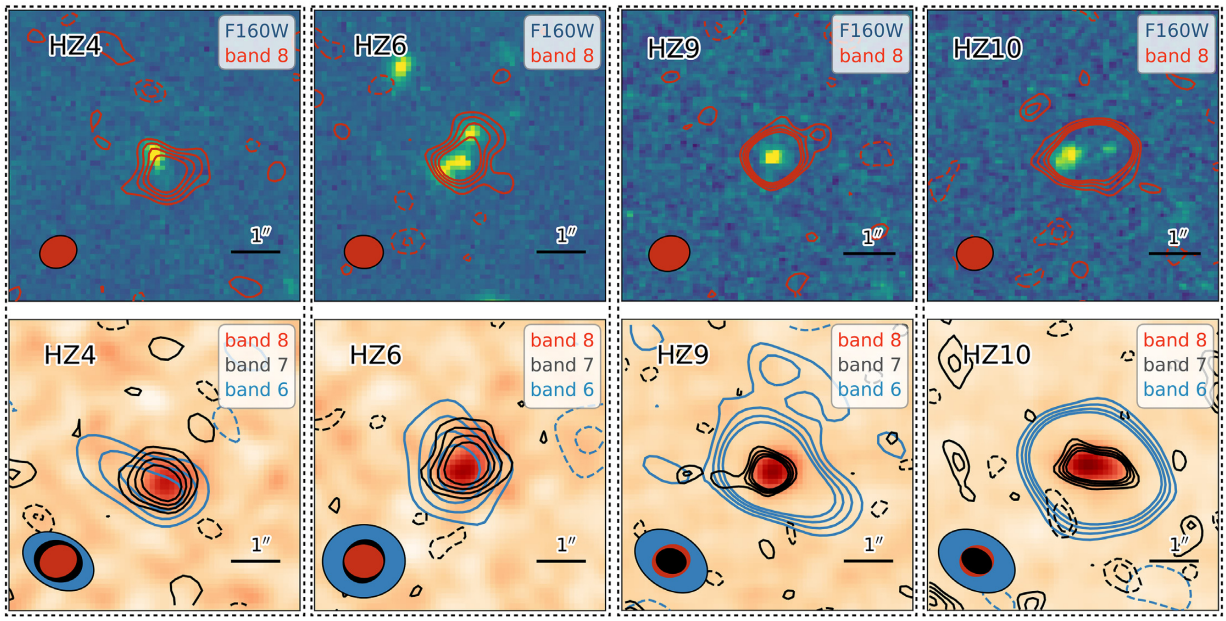

Figure 1. 6 × 6 arcsec^2 cutouts of our four sources. North is up and east is to the left. Top panels: *HST F160W* (rest-frame ∼ 2500 Å) cutouts with ALMA Band 8 continuum contours (red). Bottom panels*:* ALMA Band 8 continuum (background image) with contours showing Band 7 (black) and Band 6 (blue) continuum data from the literature. The solid contours start from 2 σ and end at 5 σ, and dashed contours indicate $-3\,\sigma$ and $-2\,\sigma$. The ALMA synthesized beams are shown for the different bands. All galaxies are significantly (5–25σ) detected in the far-IR continuum, and their flux peak positions are consistent each other within the beam sizes. There is a potential offset of the positions between the *HST* image and the far-IR detection for *HZ4*.

times for the galaxies were estimated from their 150-μm continuum luminosities and total to 1.48, 2.24, 0.64, and 0.41 h. For each target, the correlator was set up in dual polarization to cover two spectral windows of 1.875-GHz bandwidth each at a resolution of 31.25 MHz (∼ 23 km s^{-1}) in each sideband and centered at 406.4 GHz.

The Common Astronomy Software Application (`casa`) version 5.4.0 was used for data calibration and analysis. For the data calibration, we used the scripts released by the QA2 analyst (`ScriptForPI.py`). We then produced continuum maps using the `casa` task `TCLEAN` using multifrequency synthesis (`MFS`) mode with `NATURAL` weighting scheme to maximise their sensitivities. During the `TCLEAN` process, we deconvolved synthesized beam down to 3 σ, where σ is the background RMS of the image without beam deconvolution (i.e. 'dirty image'). The resulting continuum sensitivities of the Band 8 maps are 34, 40, 57, and 66 for *HZ4*, *HZ6*, *HZ9*, and *HZ10*, respectively. All sources are significantly detected (S/N ≃ 8−25) as expected from our observing strategy (top panels, Fig. 1).

2.2 Ancillary ALMA data

To measure continuum at longer wavelengths, we complemented our Band 8 observations with ancillary data available in the ALMA archive. All four sources were observed by several observing projects both in Band 6 and in Band 7. We refer interested readers to the papers listed below for more detail.

The rest-frame ∼ 200 μm (Band 6) observations are available from the ALMA project code 2015.1.00388.S (PI: N. Lu, Lu et al. 2018) and 2015.1.00928.S (PI: Pavesi, Pavesi et al. 2019) and the rest-frame ∼ 150 μm (Band 7) observations are available from the ALMA project code 2017.1.00428.L (*ALPINE*; PI: O. Le Fèvre, Le Fèvre et al. 2019; Bethermin et al. 2020; Faisst et al. 2020) for *HZ4* and for *HZ6*, and 2012.1.00523.S (PI: P. Capak, Capak et al. 2015) for *HZ9* and for *HZ10*. After we obtained data from the ALMA archive, we calibrated all data using the scripts released by the QA2 analyst (`ScriptForPI.py`). We use the appropriate versions of `casa` as specified by the scripts.

To create continuum maps, we excluded channels closer than ±3σ width of the [N II] (205 μm) or [C II] (158 μm) emission lines from the calibrated data. The emission-line frequencies and widths are taken from previous studies (Capak et al. 2015; Pavesi et al. 2018a; Bethermin et al. 2020). After masking emission lines, we create continuum maps following the same procedure as for the Band 8 data using `casa` task `TCLEAN` with `NATURAL` weighting scheme (see Section 2.1). The resulting sensitivities and synthesized beam resolutions are summarized in Table 1. All maps show significant (S/N ≃ 5–30) continuum detections, with spatial positions that are consistent across different frequencies given the beam uncertainties (bottom panels, Fig. 1).

2.3 Flux calibration errors

Given the significant detections and high flux densities measured for some of our sources, flux calibration errors are potentially a significant contributor to the overall uncertainties. We thus estimated the variability of all our flux calibrators. In particular, when flux calibrations are performed using secondary flux calibrators (i.e. quasars), we obtained the flux monitoring results from the ALMA calibrator source catalogue[4] both for Band 3 and for Band 7. We then estimated expected flux densities and errors in each observed frequency. The differences from the expected fluxes from each successive monitoring are used to estimate flux variabilities of observed frequencies. In doing so, we accounted for the typical

[4]https://almascience.eso.org/sc/

Table 2. Summary of Flux Measurements.

ID	z	$\lambda_{\rm band6}$ (μm)	$f_{\rm band6}$ (μJy)	$\lambda_{\rm band7}$ (μm)	$f_{\rm band7}$ (μJy)	$\lambda_{\rm band8}$ (μm)	$f_{\rm band8}$ (μJy)
HZ4	5.544	1294	$102 \pm 26\,(\pm 6)$	1014	$189 \pm 30\,(\pm 9)$	738	$524 \pm 88\,(\pm 31)$
HZ6	5.293	1328	$256 \pm 55\,(\pm 23)$	975	$404 \pm 61\,(\pm 18)$	738	$610 \pm 86\,(\pm 37)$
HZ9	5.541	1294	$274 \pm 22\,(\pm 18)$	1008	$570 \pm 67\,(\pm 29)$	738	$1109 \pm 84\,(\pm 67)$
HZ10	5.657	1318	$706 \pm 25\,(\pm 35)$	1027	$1519 \pm 74\,(\pm 76)$	738	$2813 \pm 129\,(\pm 169)$

Notes. Flux errors in the parentheses are calibration error estimated in Section 2.3.

measurement uncertainties of the expected flux densities. When flux calibrations are based on primary flux calibrators (i.e. solar systems objects), the flux calibrations are much less affected by the flux variabilities. Nevertheless, we applied conservative flux calibration errors of 5 per cent to take into account the potential modelling uncertainty of resolved flux calibrator observations. We estimated flux calibration errors of 6 to ~ 9 per cent for our observations (see Table 1).

3 MEASUREMENTS

3.1 Continuum flux measurements

After we confirmed individual detections in all images, we performed continuum flux density measurements in the visibility domain. While imaged maps are useful to examine the achieved sensitivities and to validate source detections, map reconstructions depend on observational and imaging parameters such as the resolution and parameters used during the deconvolution processes. The visibility domain is less affected by these parameters.

We performed visibility-based flux measurements using the task UV_FIT from the software package GILDAS[5] after creating continuum visibilities by masking emission lines, if present, following the same procedure as in Section 2.2. We used a single 2D Gaussian for visibility fitting, keeping source positions, source sizes, and integrated flux densities as free parameters. The resulting measurements for all of our sources are listed in Table 2.

3.2 IR SED fits and dust temperature

We use the Markov chain Monte Carlo (MCMC) method provided by the PYTHON package PYMC3[6] to fit the IR SEDs of our four galaxies including all the three ALMA continuum measurements described above (Table 2). The SED is parameterized as the sum of a single modified blackbody and a mid-IR power law as described in Casey (2012) (see also Blain, Barnard & Chapman 2003):

$$S(\lambda) = N_{\rm bb}\, f(\lambda; \beta_{\rm d}, T_{\rm SED}) + N_{\rm pl}\, \lambda^{\alpha}\, {\rm e}^{-(\lambda/\lambda_{\rm c})^2} \quad (1)$$

with

$$N_{\rm pl} \equiv N_{\rm bb}\, f(\lambda_{\rm c}; \beta_{\rm d}, T_{\rm SED}) \quad (2)$$

and

$$f(\lambda; \beta_{\rm d}, T_{\rm SED}) \equiv \frac{\left(1 - {\rm e}^{-(\lambda_0/\lambda)^{\beta_{\rm d}}}\right)\left(\frac{c}{\lambda}\right)^3}{{\rm e}^{(h\,c)/(\lambda\, k\, T_{\rm SED})} - 1}. \quad (3)$$

[5]GILDAS is an interferometry data reduction and analysis software developed by Institut de Radioastronomie Millimétrique (IRAM) and is available from http://www.iram.fr/IRAMFR/GILDAS/. To convert ALMA measurement sets to GILDAS/MAPPING uv-table, we followed https://www.iram.fr/IRAMFR/ARC/documents/filler/casa-gildas.pdf.
[6]https://docs.pymc.io/

In addition, the power-law turnover wavelength $\lambda_{\rm c}$ is dependent on α and $T_{\rm SED}$ (see Casey 2012). Free parameters are $N_{\rm bb}$ (normalization), α (slope of the mid-IR power law), $\beta_{\rm d}$ (emissivity index), $T_{\rm SED}$ (SED dust temperature), and λ_0 (wavelength where the optical depth is unity).

The SED dust temperature (defined by equation 1) should not be confused with the peak dust temperature, which is quoted by several observational studies (e.g. Béthermin et al. 2015; Schreiber et al. 2018). The latter is proportional to the inverse wavelength at the peak of the IR emission via Wien's displacement law,

$$T_{\rm peak}\,({\rm K}) = \frac{2.898 \times 10^3\,(\mu{\rm m\,K})}{\lambda_{\rm peak}\,(\mu{\rm m})}. \quad (4)$$

The SED and peak temperatures can be considerably different as shown in Casey (2012). Note that both are a measure of the *light-weighted* dust temperature. This is in contrast to the cold dust emitted at 25 K in the RJ tail of the far-IR spectrum ($\gtrsim$ 250 μm rest frame). This *mass-weighted* temperature is expected to be largely independent of redshift and other galaxy properties (see e.g. Scoville et al. 2016; Liang et al. 2019). We also stress that the peak temperature should not be associated with a physical dust temperature but rather with the shape of the SED. As discussed in detail in Section 4.2, several physical properties (such as opacity) can affect the wavelength at which an IR SED peaks in luminosity.

Since our data do not constrain the mid-IR part of the SED, we fix the mid-IR power-law slope to $\alpha = 2.0$. This value is the median derived in Casey (2012) from local luminous IR galaxies. However, we note that α can range between 0.5 and 5.5 depending on the amount of mid-IR emission emitted from a galaxy. We find that changing α within this range does not significantly alter our results (see Appendix A). Specifically, the peak temperature is within 5 K of the values found with a fixed $\alpha = 2$. The total IR luminosities (see derivation below) change less than 0.1 dex, which is entirely within their 1σ uncertainties (several 0.1 dex).

A largely unknown fitting parameter is λ_0, the wavelength at which the optical depth τ equals unity (i.e. optically thick at bluer wavelengths). Based on observational studies at lower redshift, it is generally assumed that $\lambda_0 \sim 200$ μm (e.g. Blain et al. 2003; Conley et al. 2011; Rangwala et al. 2011; Casey 2012; Riechers et al. 2013). However, as shown in Fig. 2, our new Band 8 observations cannot be fit with $\lambda_0 = 200$ μm for three out of four galaxies. Specifically, the two panels show rest-frame modified blackbody with mid-IR power-law models (equations 1–3 with fixed $\alpha = 2$ and $\beta_{\rm d} = 2$) for $\lambda_0 = 100$ μm (left-hand panel) and $\lambda_0 = 200$ μm (right-hand panel) for a range of SED temperatures (coloured from blue to red). The observed fluxes of our galaxies normalized to Band 6 (at 205 μm) are shown by symbols. Clearly, our Band 8 observations (at rest-frame 110 μm) cannot be explained with $\lambda_0 = 200$ μm at any reasonable temperature for all of our galaxies except *HZ6*. The emission at ~ 100 μm is therefore likely optically thin and we therefore assume

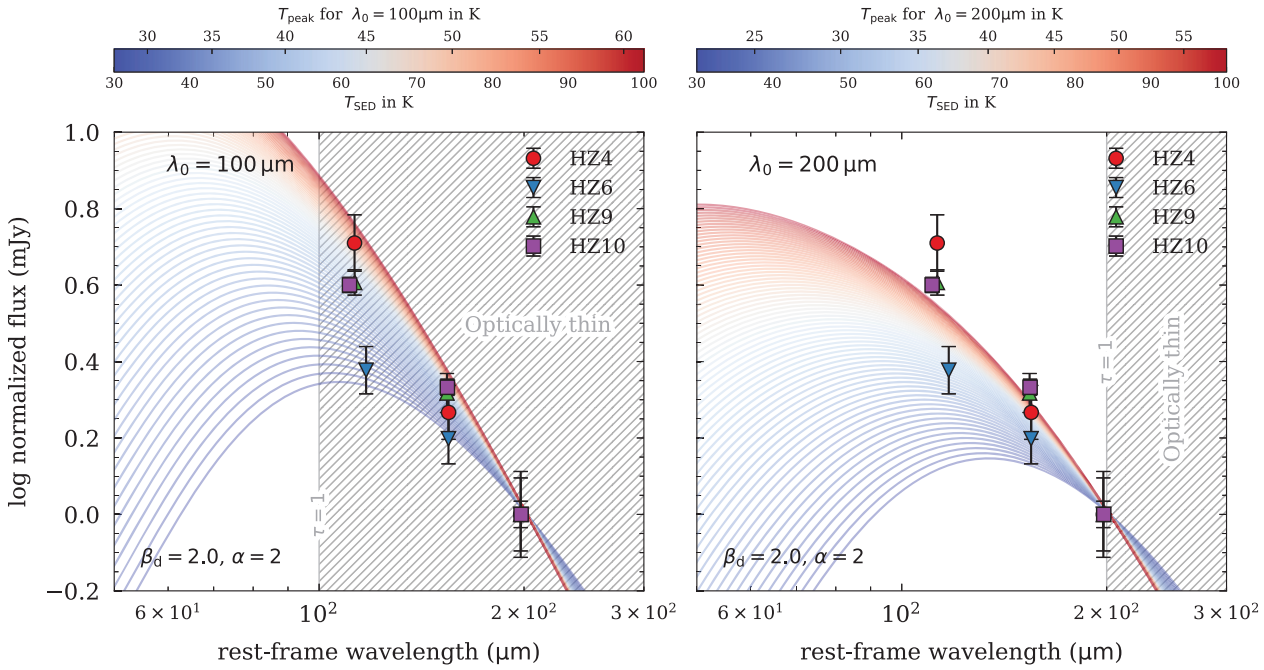

Figure 2. IR SED models assuming $\lambda_0 = 100$ μm (left-hand panel) and $\lambda_0 = 200$ μm (right-hand panel) and fixed $\alpha = 2$ and $\beta_d = 2$ for different SED temperatures from 30 K (blue) to 100 K (red). The colour bar also indicated the dust peak temperature. The continuum fluxes of all galaxies except *HZ6* can only be reproduced in the optical thin emission redward of 100 μm ($\lambda_0 = 100$ μm). This suggests optical thin dust emission. The observations are normalized to Band 6 (at 205 μm).

$\lambda_0 = 100\,\mu m$ in the following. This is consistent with theoretical models for low-opacity dust (Scoville & Kwan 1976; Draine 2006) and has also been suggested by other observational studies (Simpson et al. 2017; Dudzevičiūtė et al. 2020). In Appendix A, we fit the IR SEDs using a simple modified blackbody in the optically thin limit for comparison. We find that in this case, the peak temperatures are on average 5–10 K higher than in the non-limiting case, hence setting a hard upper limit for the temperatures.

The observations of *HZ6* can be reconciled with optically thick emission up to rest-frame 200 μm. As found in Capak et al. (2011), *HZ6* is part of a protocluster at $z = 5.3$. Specifically, *HZ6* consists of three components separated by $\Delta v < 50\,km\,s^{-1}$ in radial velocity and < 3 kpc in projected distance (Fig. 1). The components are likely gravitationally interacting and a past close passage is suggested by the diffuse rest-frame UV emission and a 'crossing time' of ~ 50 Myr. The latter is estimated using $t_{cross} \simeq (G\,\bar{\rho})^{-1/2}$, where $\bar{\rho}$ is the average mass density and G is the gravitational constant, with values based on observations ($r = 3$ kpc and total enclosed mass of $10^{10}\,M_\odot$ for a single component). This setup could cause a more optically thick medium by, e.g. the compression of gas and/or the formation of dust. With the current data, it is not possible to make further conclusions and we therefore show in the following derivations using both values of λ_0 for *HZ6*.

For the MCMC fit to the IR SEDs of our galaxies, we adopt a flat prior for the dust temperature, and a Gaussian prior for β_d with a $\sigma(\beta_d) = 0.5$ centred on 1.8 (see e.g. Hildebrand 1983). The normalization is also sampled with a Gaussian prior in linear space around an initial guess derived by the normalization in Band 7. We found that fitting in linear space is more appropriate given the errors of the data. As discussed above, α is fixed at a value of 2. To perform the fitting, we use the *No-U-Turn Sampler* (Hoffman & Gelman 2011), which is an extension to the Hamilton Monte Carlo algorithm (Neal 2012) and is less sensitive to tuning. We draw 18 000 samples in total with a target acceptance of 0.99, which we found to provide the best performance.

Fig. 3 shows the best-fitting IR SEDs together with the 1σ uncertainties for each of our galaxies. Thanks to our Band 8 data at rest-frame wavelengths of 110 μm, we can put more stringent constraints on the location of the peak of the IR SED. The galaxies *HZ4* and *HZ6* are fainter, resulting in larger uncertainties of the fit. While the mid-IR blueward of the peak is poorly constrained, the RJ tail (at > 1000 μm observed frame) can be robustly extrapolated based on our data. The individual and stacked best-fitting IR SEDs are available in the online version or on request.

Fig. 4 shows the derived SED (left-hand panel) and peak (middle panel) dust temperature as well as total IR luminosity (right-hand panel) contours (1σ) as a function of the emissivity index β_d for our four galaxies. We find emissivity indices between 1.6 and 2.4 for all galaxies, with a median of 2.0, which is consistent with measurements at lower redshifts (e.g. Conley et al. 2011; Casey 2012). The dust SED temperatures range between 40 and 60 K with a median at 48 K. For the dust peak temperatures, we find a range of 30–43 K with a median of 38 K. The total IR luminosities (L_{IR}) are derived by integrating the best-fitting SED between3−1100 μm and range 5–30 $\times\ 10^{11}\,L_\odot$. We also quote far-IR luminosities (L_{FIR}) measured by integrating the flux between 42.5 and 122.5 μm for easier comparison with the literature. All measurements are summarized in Table 3.

3.3 Molecular gas masses from the RJ dust continuum

The measurement of molecular gas masses of galaxies is crucial to understand the star formation processes determining their growth and evolution. Low-J transitions of the CO molecule are used regularly at $z < 2$ (e.g. Tacconi et al. 2010; Genzel et al. 2015; Freundlich et al.

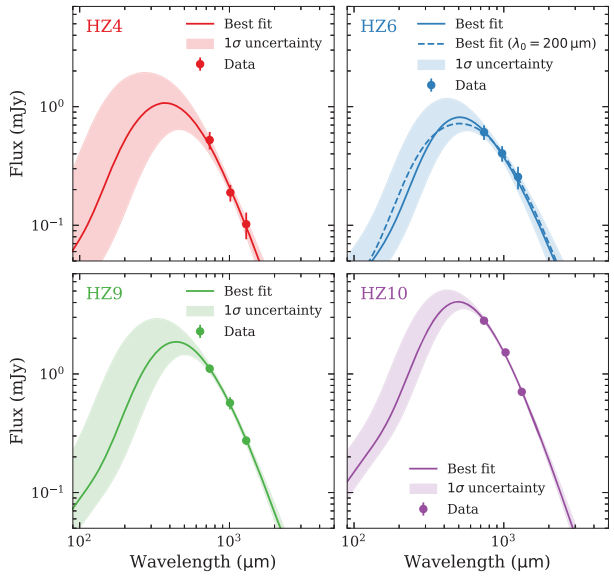

Figure 3. Best-fitting IR SEDs for the four galaxies derived from equations (1) to (3) (1σ uncertainty indicated by coloured band). The wavelength is given in observer frame. The dashed line shows the case with $\lambda_0 = 200$ μm for *HZ6*. The new Band 8 continuum measurements (110 μm rest frame, 740 μm observed) probe better the peak of the IR SED, which allows us to put the first constraints on the dust temperature and total IR luminosity at these redshifts. Note that the scale of the *y*-axis is the same in all panels to show the differences in total flux. The individual and stacked best-fitting IR SEDs are available in the online version or on request.

2019), but this is not feasible for large samples of normal galaxies at higher redshifts due to the large amount of necessary telescope time. Currently, only very few observations of CO in normal galaxies at $z > 5$ exist (D'Odorico et al. 2018; Pavesi et al. 2019). Alternatively, the far-IR [C II] emission line can be used as tracer of molecular gas (De Looze et al. 2014; Zanella et al. 2018; Dessauges-Zavadsky et al. 2020), however, there are considerable uncertainties in its use due to the unknown origin of C^+ emission.

Alternatively, molecular gas masses can be measured using the dust continuum emission emitted at rest-frame 850 μm in the RJ tail of the far-IR spectrum (Scoville et al. 2014, 2016, 2017; Hughes et al. 2017; Kaasinen et al. 2019; Dessauges-Zavadsky et al. 2020). For current samples of main-sequence galaxies at high redshifts, the far-IR slope (defined by the emissivity index β_d) cannot be constrained directly due to the lack of observations. Significant assumptions have therefore to be made to quantify the rest-frame 850-μm continuum. With our three-band data sampling the SED redward of the far-IR peak, we can constrain the far-IR slope for the first time at these redshifts directly. The molecular gas masses are then derived using the observed flux at rest-frame 205 μm (Band 6, $S_{\nu_{obs}}$ in mJy[7]) that is extrapolated to 850 μm using the full probability distribution of β_d from our MCMC fit and equation (16) in Scoville et al. (2016) with similar assumptions:

$$M_{mol} = 1.78\, S_{\nu_{obs}}\, (1+z)^{-(3+\beta_d)} \left(\frac{\nu_{850\mu m}}{\nu_{obs}}\right)^{2+\beta_d} D_L^2(z) \times \left(\frac{6.7\times10^{19}}{\alpha_{850}}\right)\left(\frac{\Gamma_{RJ,z=0}}{\Gamma_{RJ}}\right) \times 10^{10}\,M_\odot.$$

In this case, $D_L(z)$ is the luminosity distance at redshift z in Gpc and we assume $\alpha_{850} = 6.7 \times 10^{19}$ erg s^{-1} Hz^{-1} M$_\odot^{-1}$, which is the average measured for galaxies at $z < 3$ (Scoville et al. 2016). $\Gamma_{RJ}(\nu_{obs}, T_d, z)$ is the correction for departure in the rest frame of the Planck function from RJ and depends on the *mass-weighted* dust temperature (different from T_{SED} or T_{peak}, which are *luminosity-weighted* temperatures). For the latter, we adopt 25 K, but assuming higher temperatures such as 35 K lowers the inferred molecular masses by less than 10 per cent.

The left-hand panel of Fig. 5 shows the derived 1σ contours of the molecular masses for our galaxies from our MCMC fit. The masses range between $0.3-8.0 \times 10^{10}$ M$_\odot$. The middle panel shows the molecular gas fractions ($f_{gas} = M_{mol}/(M_{mol} + M_{stellar})$, using stellar masses from Capak et al. (2015), summarized in Table 3), which range between 30 and 80 per cent. Statistically, this is consistent with the *ALPINE* sample at $z = 5.5$ (Dessauges-Zavadsky et al. 2020). This is expected as our galaxies are consistent with the average masses and SFRs of the *ALPINE* sample (see Faisst et al. 2020). The right -hand panel of Fig. 5 compares the dust continuum gas masses with the difference between dynamical and stellar masses. This difference should yield total gas masses modulo the contribution of dark matter, which is expected to be of the order of 10–20 per cent or less at the radii probed here (Barnabè et al. 2012). The dynamical masses are derived inside a half-light radius from the [C II] emission-line velocity profile (Pavesi et al. 2019). Generally, we find an agreement within a factor of 2 ($<1\sigma$) between gas masses derived from dust continuum and dynamical masses. However, assuming $\lambda_0 = 100$ μm for the fit of *HZ6* results in a 2σ discrepancy. As noted earlier, *HZ6* is a three-component major merger system with significant gravitational interaction. The complex velocity structure likely causes large uncertainties in its dynamical mass estimate. In addition, the 850-μm-continuum derived gas mass encompasses the whole extended system, while the dynamical mass captures only a fraction of the gas. Both can explain its larger offset from the one-to-one line compared to the other galaxies. On the other hand, if the dynamical mass is reliable, this indicates once more that the emission in *HZ6* could be optically think up to 200 μm (as $\lambda_0 = 200$ μm results in discrepancy).

Pavesi et al. (2019) report a gas mass estimate from CO(2 − 1) emission for *HZ6*[8] and *HZ10*, assuming a Milky Way-like CO to molecular gas conversion factor ($\alpha_{CO} = 4.5\,M_\odot/(K\,km\,s^{-1}\,pc^2)$) and brightness temperature ratio $R_{21} = 1$. They find 1.3×10^{11} M$_\odot$ for *HZ10* and a limit $< 2 \times 10^{10}$ M$_\odot$ for *HZ6* (see Fig. 5). The CO-gas mass estimate of *HZ10* is a factor of 2.5 larger ($\sim1\sigma$ discrepancy) than what we measure from dust continuum and dynamical masses. The upper limit in CO-derived gas mass for *HZ6* is consistent with our measurement if assuming $\lambda_0 = 200$ μm (but not if optically thin dust at 100 μm). The discrepancy of the measurements for *HZ10* are not significant, given the large measurement errors as well as uncertainties in α_{CO} and the brightness temperature ratio. However, large α_{CO} values above 20 that are expected for metal-poor environments such as in the Small Magellanic Cloud (see Leroy et al. 2011) can be excluded for *HZ10*. This is in agreement with earlier studies that suggest that *HZ10* is fairly metal enriched, even close to solar metallicity, based on its strong rest-frame UV absorption lines (e.g. Faisst et al. 2017; Pavesi et al. 2019). Clearly, larger samples or more precise measurements have to be obtained in order to draw final conclusions.

[7]Note that the dust is likely optically thin at this wavelength, *cf.* Fig. 2.

[8]This galaxy is named *LBG-1* in their paper, see also Riechers et al. (2014).

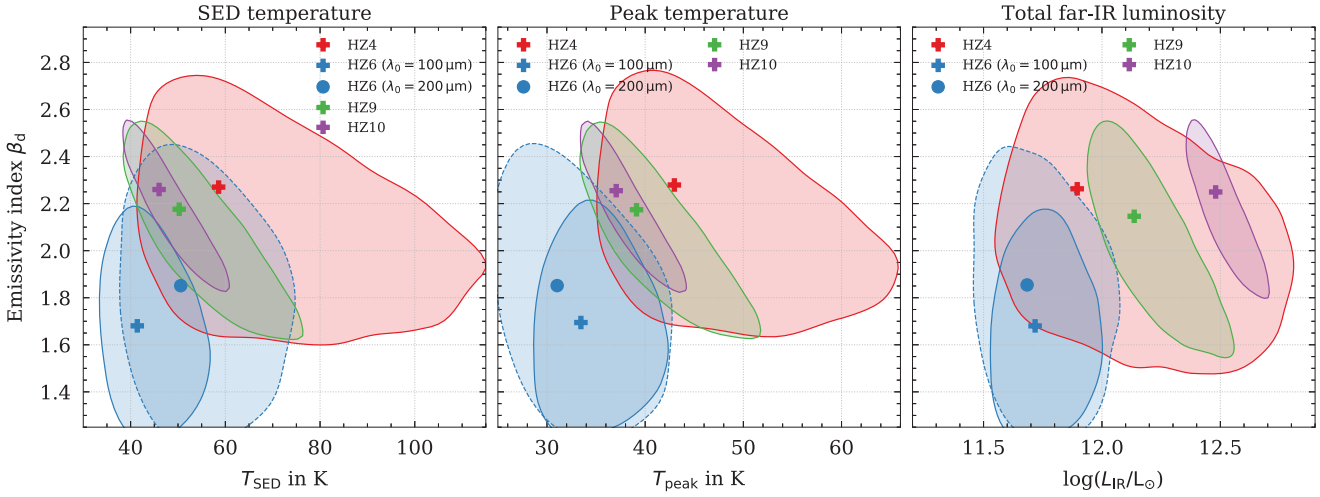

Figure 4. 1σ contours derived from the MCMC Bayesian analysis using the PyMC3 package of the SED (left-hand panel) and peak (middle panel) dust temperature as well as the total (3−1100 μm) IR luminosity (right-hand panel) as a function of the emissivity index β_d. The dashed contour shows the results for *HZ6* in the optically thick case ($\lambda_0 = 200$ μm). Band 8 probes the wavelength close to the far-IR peak for our galaxies, hence allows us to put first constraints on dust temperatures at these redshifts.

Table 3. Summary of properties derived from the IR and UV/optical. All IR-derived quantities (except β_d) are computed by marginalizing over β_d. The quoted errors include all uncertainties and are 1σ.

ID	β_d	T_{SED} (K)	T_{peak} (K)	log(L_{IR})^a (L$_\odot$)	log (L_{FIR})^b (L$_\odot$)	log(M_{ISM}) (M$_\odot$)	f_{ISM}	log (SFR$_{IR}$)^c (M$_\odot$ yr^{-1})	log (SFR$_{UV}$)^d (M$_\odot$ yr^{-1})	t^e_{depl} (Myr)	log (M_*)^f (M$_\odot$)
HZ4	$2.01^{+0.69}_{-0.57}$	$57.3^{+67.1}_{-16.6}$	$42.4^{+28.7}_{-8.2}$	$11.91^{+0.37}_{-0.91}$	$11.83^{+0.44}_{-0.23}$	$9.92^{+0.43}_{-0.50}$	$0.67^{+0.21}_{-0.31}$	$1.89^{+0.37}_{-0.91}$	$1.47^{+0.05}_{-0.05}$	88^{+243}_{-63}	$9.67^{+0.21}_{-0.21}$
HZ6	$1.60^{+0.58}_{-0.57}$	$40.8^{+17.8}_{-7.2}$	$33.9^{+9.9}_{-5.9}$	$11.73^{+0.22}_{-0.34}$	$11.52^{+0.24}_{-0.31}$	$10.55^{+0.43}_{-0.45}$	$0.73^{+0.17}_{-0.26}$	$1.72^{+0.22}_{-0.34}$	$1.54^{+0.03}_{-0.03}$	442^{+845}_{-293}	$10.17^{+0.15}_{-0.15}$
HZ6^g	$1.85^{+0.69}_{-0.82}$	$48.4^{+30.2}_{-10.8}$	$30.8^{+15.4}_{-6.5}$	$11.69^{+0.26}_{-0.51}$	$11.50^{+0.29}_{-0.43}$	$9.99^{+0.78}_{-0.62}$	$0.37^{+0.49}_{-0.30}$	$1.68^{+0.26}_{-0.51}$	$1.54^{+0.03}_{-0.03}$	143^{+116}_{-512}	$10.17^{+0.15}_{-0.15}$
HZ9	$2.01^{+0.52}_{-0.70}$	$49.4^{+29.0}_{-10.7}$	$38.9^{+13.7}_{-5.8}$	$12.14^{+0.21}_{-0.45}$	$11.94^{+0.21}_{-0.33}$	$10.39^{+0.44}_{-0.35}$	$0.81^{+0.13}_{-0.19}$	$2.13^{+0.21}_{-0.45}$	$1.14^{+0.05}_{-0.05}$	181^{+392}_{-122}	$9.86^{+0.23}_{-0.23}$
HZ10	$2.15^{+0.41}_{-0.54}$	$46.2^{+16.2}_{-8.5}$	$37.4^{+8.0}_{-4.9}$	$12.49^{+0.15}_{-0.25}$	$12.28^{+0.15}_{-0.21}$	$10.72^{+0.36}_{-0.26}$	$0.70^{+0.17}_{-0.16}$	$2.48^{+0.15}_{-0.25}$	$1.56^{+0.06}_{-0.06}$	168^{+194}_{-91}	$10.39^{+0.17}_{-0.17}$

Notes. [a]Total IR luminosity computed in the range from 3 to 1100 μm.
[b]Total far-IR luminosity computed in the range from 42.5 to 122.5 μm.
[c]The IR SFR is derived from the total IR luminosity (L_{IR}) using the relation given in Kennicutt (1998).
[d]The rest-UV SFR is derived from the rest-UV luminosity published in Capak et al. (2015) using the relation given in Kennicutt (1998).
[e]The depletion time is defined as M_{ISM}/SFR$_{tot}$, where SFR$_{tot}$ is the total SFR equal to the sum of the IR and rest-UV SFRs.
[f]Stellar masses are taken from Capak et al. (2015). They are derived from SED fitting to the photometry available on the COSMOS field using `Le Phare` (Arnouts et al. 1999; Ilbert et al. 2006). We refer to Capak et al. (2015) for more details.
[g]Measurement with $\lambda_0 = 200$ μm, see the text for more details.

From the total IR luminosity (L_{IR}), we can derive IR SFRs using the Kennicutt (1998) relation. Together with the (not dust obscuration corrected) rest-UV SFRs [derived from the UV luminosities given in Capak et al. (2015) and the Kennicutt (1998) relation], we can compute the total SFRs of the galaxies. The different SFRs for our galaxies are summarized in Table 3. Using the total SFRs of the galaxies, we can derive gas depletion times via $t_{depl} = M_{mol}$/SFR$_{tot}$. For *HZ4*, *HZ9*, and *HZ10* find values between 88 and 181 Myr. This is in agreement with the trend of decreasing depletion time with higher redshifts (e.g. Scoville et al. 2016). For *HZ6*, the depletion time depends on the assumed λ_0. For λ_0 equal to 100 and 200 μm, we derive a depletion time of 442 and 143 Myr, respectively.

4 DISCUSSION

4.1 Rising temperature towards high redshifts?

Fig. 6 puts our measurements at $z \sim 5.5$ into context with measurements from the literature at $z < 4$ and $z > 6$. At $z = 0$, we show peak temperature measurements derived in Faisst et al. (2017, using equations 1–3) for the KINGFISH sample (Skibba et al. 2011), the *Dwarf Galaxy Sample* (DGS, Madden et al. 2013), and the GOALS sample (Kennicutt et al. 2011). The data for Arp220 is taken from Rangwala et al. (2011). At $z = 0.2$−4.0 from the *ALMA LABOCA ECDFS Sub-mm Survey* (*ALESS*, da Cunha et al. 2015), the sample from Béthermin et al. (2015), and galaxies at from Magnelli et al. (2014). For the latter, we select a similar range in total IR luminosity as our sample [log (L_{IR}/L$_\odot$) ∼ 10.5–12.5]. We also note that the stellar mass range is similar to our sample. At $z > 6$, we show galaxies from Bakx et al. (2020, lower limit), Knudsen et al. (2016), and Hashimoto et al. (2019). For the latter two, we have re-measured the peak temperature with our method. The trend derived from hydrodynamic simulations (Liang et al. 2019; Ma et al. 2019) is shown as dot–dashed line.

Our measurements at $z \sim 5.5$ show elevated dust temperatures compared to average local galaxies such as from the KINGFISH sample. Taking the uncertainties into account, we can exclude peak temperatures of less than 30 K. The median peak temperature

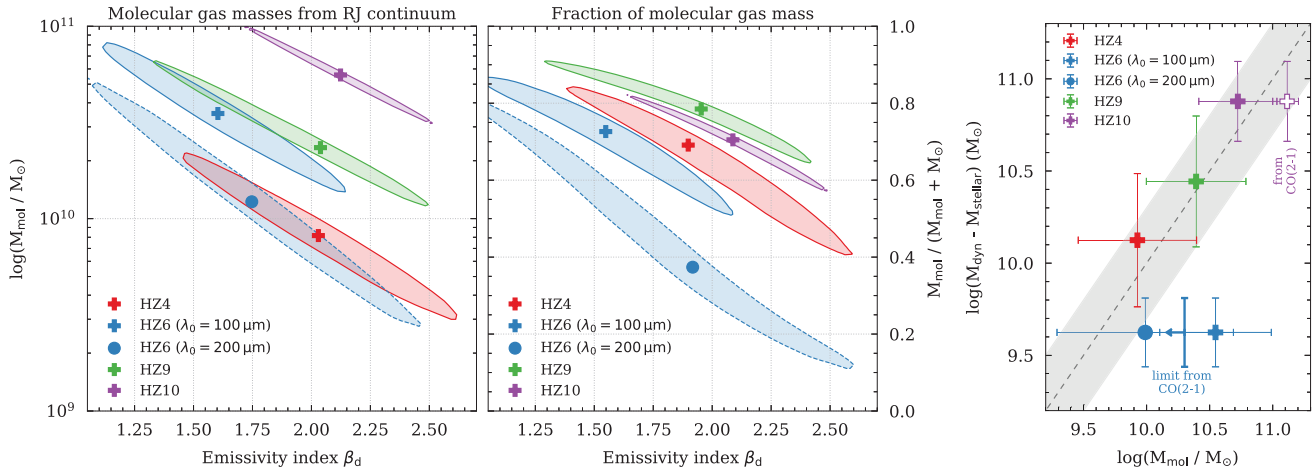

Figure 5. 1σ contours derived from the MCMC Bayesian analysis using the PyMC3 package of the molecular gas masses (left-hand panel) and fractions (middle panel) as a function of the emissivity index β_d. The molecular gas masses have been estimated using the RJ dust continuum at rest-frame 850 μm using the method by Scoville et al. (2016). The three ALMA continuum frequencies put the first robust constraints on the emissivity index (far-IR slope) at these high redshifts, which is critical to derive molecular gas masses. The right-hand panel shows the comparison of our dust-continuum derived molecular gas masses and the difference between dynamical and stellar mass (expected to be equal to the total gas mass modulo dark matter). The grey region shows a factor of 2 (0.3 dex) deviation from the one-to-one line. Note that *HZ6* (blue) has a complicated velocity structure due to its major merger nature, which makes the measurement of its dynamical mass significantly uncertain. The molecular gas mass measurements obtained from the CO(2 − 1) transition (Pavesi et al. 2019) are also shown for comparison. They largely agree with our measurements.

measured for our galaxies is at 38 ± 5 K, with a low-probability tail towards higher temperatures (Fig. 4). However, although the temperatures at $z \sim 5.5$ are higher compared to average local galaxies, we find that our values are about 10 K below what would be predicted from an extrapolation of observational data at $z < 4$ at similar IR luminosities. Particularly, the Schreiber et al. (2018) IR SED template at $z = 4$ suggests a peak temperature of 42 K. If extrapolated to $z = 5.5$, this results in ~ 46 K, which is ~ 10 K higher than what we measure from our data (at similar IR luminosity). On the other hand, our measurements are consistent with the empirically derived IR SED of $4 < z < 6$ galaxies from Bethermin et al. (2020), who find an average peak temperature of 38 K. Furthermore, we find similar peak temperatures as reported at $z > 6$ by the various studies.

Summarizing, the peak temperatures of high-z galaxies are warmer compared to average local galaxies, which has to be taken into account when parameterizing the IR SEDs of these galaxies. However, our observational data suggest that the peak temperature (i.e. the wavelength at peak emission of the IR SED) does not evolve anymore strongly beyond redshifts $z = 4$ for a fixed total IR luminosity. This behaviour is reproduced in hydrodynamic simulations (e.g. Liang et al. 2019; Ma et al. 2019), which show a flattening of the temperature evolution with redshift for galaxies selected with $L_{IR} > 10^{11}$ L$_\odot$ (Fig. 6).

4.2 Explaining the observed $T_{peak}(z)$ evolution with an analytical model of a spherical dust cloud

In the previous section, we have constrained the evolution of the peak temperature with redshift. Our unique observations at $z \sim 5.5$ and literature data at lower redshifts suggest that the temperature rises up to $z \sim 4$ and then tends to flatten off. At this point, we note that the increase in SED or peak temperature with redshift is merely a statement on a shift in the wavelengths at which the IR SED peaks, i.e. its *shape*. This shift can be due to several physical reasons, including changes in the UV luminosity of a central source (i.e. the young stars), the dust mass density or the opacity of the dust. Such dependencies have been seen observationally in the local galaxy samples (Fig. 6). For example, the KINGFISH sample [consisting of mostly solar metallicity and IR fainter ($10^{10}-10^{11}$ L$_\odot$) galaxies] shows peak temperatures between 20 and 30 K. On the other hand, the IR luminous ($10^{11}-10^{12}$ L$_\odot$) GOALS sample (also close to solar metallicity) shows higher average peak temperatures (25–40 K). The DGS sample shows similarly high peak temperatures as the GOALS sample at less than a tenth solar metallicity and $L_{IR} < 10^{11}$ L$_\odot$. This suggests that metallicity and IR luminosity have a significant effect on the peak temperature measured by the observer: High peak temperatures do not only occur in IR luminous galaxies but also in IR faint galaxies with low metallicity (see also fig. 4 in Faisst et al. 2017). Explaining this trend is not simple given the complex relations between different physical and structural parameters of galaxies on many levels (see also review by Calzetti 2001). At high IR luminosities, dust may be heated by the internal source (e.g. young stars) causing the emission of light at bluer wavelengths (hence resulting in warmer peak temperatures). On the other hand low-metallicity environments alter the dust properties such as, for example, result in smaller dust grain sizes or more diffuse molecular gas clouds (Pak et al. 1998; Misselt, Clayton & Gordon 1999) and lower dust-to-gas ratios (e.g. Issa, MacLaren & Wolfendale 1990; Lisenfeld & Ferrara 1998). Lower opacity would allow us to see dust emission at shorter wavelengths, thus shifting the peak temperature to higher values.

These physical relations can cause selection effects (such as a survey limit in total IR luminosity) make a positive relation between temperature and redshift more pronounced (see discussion in Dudzevičiūtė et al. 2020). However, as shown in table 1 of Schreiber et al. (2018), even at a fixed total IR luminosity, the trend of increasing peak temperatures from 25 to 40 K at $z = 1.0$–3.5 persists. This is indicated by the small dark-blue open circles in Fig. 6, which show the average peak temperature from these data in *matched* bins of IR luminosity.

In the following, we use a simple analytical model to investigate how the output of UV photons from a dust-enshrouded source

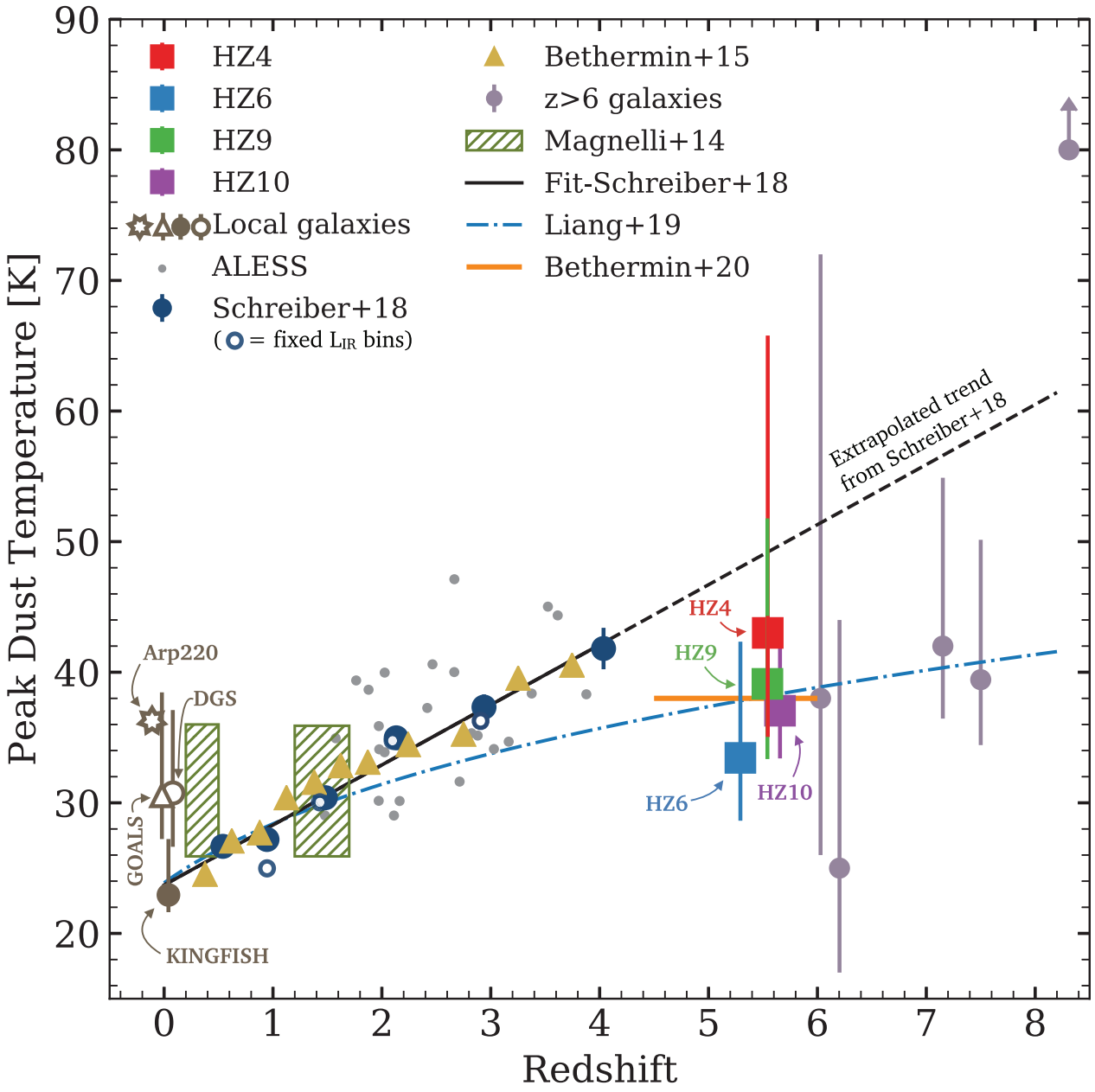

Figure 6. Peak dust temperature (T_{peak}) evolution with redshift. The large coloured squares show our galaxies at $z \sim 5.5$. We also show galaxy samples at $z = 0$ from the KINGFISH (dark grey circle), DGS (dark grey open circle), and GOALS (dark grey open triangle) samples (shifted by 0.02 in redshift for clarity), and galaxies at $z = 0.2-4.0$ (matched to our luminosity range) from *ALESS* (grey small circles, da Cunha et al. 2015), Béthermin et al. (yellow triangles, 2015), and Magnelli et al. (hatched rectangles, 2014), as well as $z > 6$ (light purple circles, Knudsen et al. 2016; Hashimoto et al. 2019; Bakx et al. 2020). The data for Arp220 is taken from Rangwala et al. (2011). For consistency, we re-measured the T_{peak} of the local galaxies as well as $z > 6$ galaxies with our method (see Section 3). The latter include CMB correction. The fit to the Schreiber et al. (2018) data (large dark-blue circles) is shown in black (dashed when extrapolation) and the small dark-blue open circles show these data binned in matching bins of infrared luminosity. In addition, we show the expected peak temperature evolution from hydrodynamic simulations (blue dot–dashed, Liang et al. 2019; Ma et al. 2019), and the temperature derived from an average template for *ALPINE* galaxies (orange line, Bethermin et al. 2020). Galaxies at $z > 4$ have warmer peak temperatures compared to average local galaxies, however, are 5–10 K cooler than what would be predicted from the trend found at $z < 4$. This indicates a flattening of the $T_{peak}-z$ relation at $z > 4$, which could be due to a lower dust abundance or opacity in high-redshift galaxies.

(specifically the ratio between UV luminosity and dust mass) and the density of dust (i.e. the dust opacity) affect the shape of the IR SED and with it the emergent peak temperature measured by an external observer.

We model the emitted heat (and hence peak temperature) from a dust cloud around stars using a model based on Scoville & Kwan (1976) that will be described in a forthcoming work (Scoville et al., in preparation). The model assumes a central source of UV light enshrouded in a dust cloud with spherical symmetry and constant density, and calculates the heating in concentric shells of dust mass. Secondary heating (from re-emitted light) is included, as well as the increased background temperature by CMB heating at high

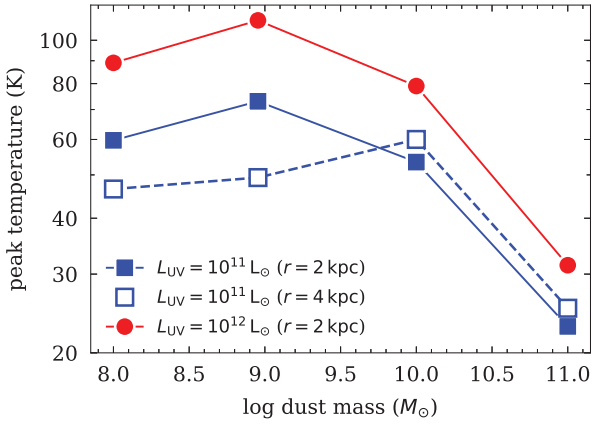

Figure 7. Dependence of peak temperature of emergent light on dust mass and central UV luminosity based on a symmetric shell model (Scoville et al., in preperation). The model assumes two different radii of the spherical dust cloud (2 and 4 kpc) and two intrinsic UV luminosities (10^{11} and 10^{12} $L_\odot$) of the embedded source. Due to the fixed size of the dust cloud, the dust volume density, and dust opacity increase to the right. The temperature drops at high dust masses (high opacity) because the hotter dust becomes optically thick. The temperature ceases to rise at a dust mass density of 3×10^7 M$_\odot$ kpc^3 independent of UV luminosity.

redshift. The latter, however, does not affect the dust temperature below $z = 6$ significantly. In the following, we consider models for different intrinsic (i.e. obscured plus unobscured) UV luminosities and dust cloud radii. For the UV luminosity, we choose 10^{11} and 10^{12} L$_\odot$, which is expected for our galaxies assuming that the intrinsic UV luminosity equals the total emitted IR luminosity (energy conservation). For the radius, we assume 2 and 4 kpc, consistent with the sizes of far-IR emission observed for our galaxies (∼0.5 arcsec at $z = 5.5$).

Fig. 7 shows the peak temperature of the spectrum of emergent light computed for our different models as a function of dust mass. Note that dust mass in this case directly corresponds to dust density, hence opacity, as the radius of the cloud is fixed. This figure shows several trends. First, the change in peak temperature as a function of UV luminosity is apparent. Specifically, increasing the UV luminosity by an order of magnitude increases the temperature by a factor of ∼1.6. This is expected because $T_{peak} \propto L_{UV}^{1/5}$ for emissivity varying as λ^{-1} and optically thin dust at the far-IR peak. Secondly, for a given UV luminosity, the peak temperature increases for decreasing opacity (i.e. dust mass or density). This can be explained by the fact that hot dust at the peak of the IR SED becomes visible to the observer as the opacity drops. At a certain value of opacity, the temperature ceases to rise. For a dust cloud radius of 2 kpc (4 kpc), this is reached at a dust mass of 10^9 M$_\odot$ (10^{10} M$_\odot$), which translates into an *average* dust mass density of $\bar{\rho}_d \sim 3 \times 10^7$ M$_\odot$ kpc^{-3}. Note that this number is independent of the intrinsic UV luminosity of the dust-enshrouded source.

Taking the output of this model at face value, the general increase of dust peak temperature with increasing redshift (at roughly fixed total IR luminosity) can be explained by a decreasing dust opacity, which causes hot dust at short wavelengths to become optically thin and therefore visible to ALMA. In fact, several observations point in this direction. For example, the blue UV continuum slopes of galaxies in the early Universe suggest that UV light is less attenuated by dust (e.g. Bouwens et al. 2014). At the same time, the fraction of dust-obscured star formation decreases significantly at $z > 4$ (Fudamoto et al. 2020). The current lack of galaxies observed with very hot

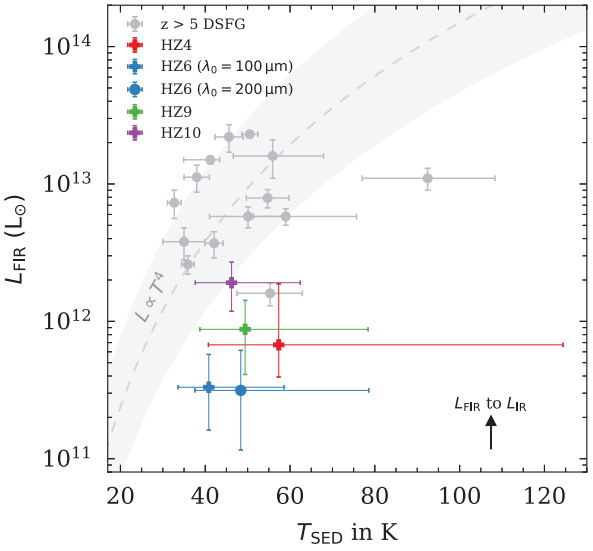

Figure 8. Comparison of SED temperature and far-IR luminosity (L_{FIR}) to a sample of DSFGs at $z > 5$ from Riechers et al. (2020). The luminosity is measured consistently between 42.5 and 122.5 μm (the arrow shows the difference to L_{IR}). Our galaxies fall off the $L \propto T^4$ relation (here normalized median luminosity and temperature of the DSFGs with 0.5 dex range indicated). For a given luminosity, they are warmer than expected from this relation. This offset may be caused by different dust abundances, dust surface densities, or dust opacities between DSFGs and normal galaxies.

temperatures at $z > 5$ (that would be expected by the trends found at $z < 4$) can also be motivated by our model. As the dust opacity (i.e. dust mass density) continues to decrease at higher redshifts, the hot dust becomes optically thin and its temperature ceases to rise (Fig. 2). In our model, this happens at an average dust mass density of 3×10^7 M$_\odot$ kpc^{-3}. This is indeed in similar to what is expected for our galaxies: Assuming an average molecular gas mass of 3×10^{10} M$_\odot$ (Section 3.3), a gas-to-dust ratio of 100, and an average size of 2 kpc, we estimate a dust mass density of $\sim 10^7$ M$_\odot$ kpc^{-3}.

4.3 Comparison with dusty star-forming galaxies at $z > 5$

In Fig. 8, we compare the far-IR luminosity and SED temperatures of our galaxies to a compilation of IR luminous dusty star-forming galaxies (DSFGs) at $z > 5$ from Riechers et al. (2020) from the CO Luminosity Density at High Redshift survey (COLDz, Pavesi et al. 2018b; Riechers et al. 2019). For a fair comparison, we show SED dust temperatures and far-IR luminosities (L_{FIR}[9]). One would expect that for an increasing far-IR luminosity, the dust temperature increases (cf. Fig. 7). This is indicated by the $L \propto T^4$ relation (optically thick case) normalized to the median of the DSFGs,

$$L_{FIR} = 9.4 \times 10^{12} \left(\frac{T_{SED}}{50.1}\right)^4 \text{L}_\odot. \quad (5)$$

However, our galaxies seem to be significantly warmer than predicted by this relation, or, for a given temperature their far-IR luminosity is too faint. Formulated in a different way, over 2.5 orders of magnitudes in IR luminosity, the peak dust temperature is constant, which is in direct contradiction to what is found in the local Universe (e.g. Magnelli et al. 2014). Since the galaxies are at similar redshifts, this indicates a fundamental difference in the dust properties of

[9]For our sample, we find that $\log(L_{FIR}/L_\odot) \simeq \log(L_{IR}/L_\odot) - 0.2$.

in the two samples. Capitalizing on the previous sections and our analytical model, a higher dust abundance and/or dust surface density in the DSFGs would explain the observed differences. Furthermore, as mentioned above and in Faisst et al. (2017), metallicity (likely connected to dust opacity) has a strong impact on the SED and peak dust temperature. A lower metallicity in our galaxies compared to the DSFGs would increase their temperature at a fixed far-IR luminosity and push them off the $L \propto T^4$ relation.

4.4 A final note on implication on $L_{\rm IR}$ measurements

The evolution of the shape of the IR SED with redshift has important consequences on the measurement of the total IR luminosity. This quantity is important in several ways, for example, for the computation of dust masses and total SFRs or the dust properties of high-redshift galaxies via the study of the IRX$-\beta$ relation. For surveys such as *ALPINE*, which target large numbers of main-sequence high-redshift galaxies, only one far-IR data point at 150 μm exists per galaxy. The above quantities therefore depend strongly on the assumed shape of the IR SED ($\beta_{\rm d}$, α, and temperature). Using the three-band constraints on the IR SEDs of our four galaxies, we can test previous measurements of the total IR luminosity that are based on only the 150-μm continuum data point.

We derive total IR luminosities between $\log(L_{\rm IR}) = 11.7 - 12.5$ for our galaxies (Table 3). Previously obtained luminosities by Capak et al. (2015), based on 150-μm continuum only, also assumed equation (1), however, a lower temperature prior ($T_{\rm SED} = 25$–45 K or $T_{\rm peak} = 20$–30 K) and $\lambda_0 = 200$ μm, but consistent emissivity range ($\beta_{\rm d} = 1.2-2.0$). With these assumptions, $L_{\rm IR}$ would be underestimated consistently by $0.3-0.6$ dex (factors of $2-4$). In Bethermin et al. (2020), an average IR SED created from stacked photometry of COSMOS galaxies between $4 < z < 6$ is normalized to the 150-μm data points of the *ALPINE* galaxies to derive their total luminosities. This approach leads to consistent total IR luminosities with ours within less than 0.2 dex (< 60 per cent difference). This result is also reflected in the good agreement of $T_{\rm peak}$ between their average IR SED and our best fits (cf. Fig. 6). This comparison shows that (at least statistically) the total IR luminosities of the *ALPINE* sample derived in Bethermin et al. (2020) are reasonable and highlights the importance of temperature assumptions in deriving this quantity.

5 CONCLUSIONS

We have acquired ALMA Band 8 data for four galaxies at $z \sim 5.5$ to put improved constraints on their IR SEDs, specifically their peak dust temperatures, total IR luminosities, and molecular gas masses. The continuum measurements at a rest-frame wavelength of ~ 110 μm are blueward of other measurements from the literature in Band 6 (~ 200 μm) and Band 7 (~ 150 μm), and therefore extend the baseline towards the peak of IR emission. The IR SEDs are fit using a modified blackbody with mid-IR power law. The peak temperature is derived using Wien's law and the molecular gas masses are measured using the extrapolated 850-μm continuum emission. The measurement of the latter benefits from our so far strongest constraints on the dust emissivity index $\beta_{\rm d}$ at these high redshifts. In the following, we summarize our findings as follows:

(i) The best-fitting peak temperatures range at 30–43 K (median of 38 K, Fig. 4). These temperatures are warmer compared to average local galaxies but ~ 10 K lower than what would be predicted from trends at $z < 4$ at similar IR luminosities. Our measurements are consistent with the most recent hydrodynamical zoom-in simulations, as well as measurements at $z > 6$.

(ii) We find dust emissivity indices ($\beta_{\rm d}$) between 1.6 and 2.4 with a median of 2.0 (Fig. 4) for our galaxies, consistent with measurements at lower redshifts.

(iii) Our new Band 8 data suggest that the emission between rest-frame 100–200 μm is optically thin (i.e. can be fit with $\lambda_0 = 100$ μm) for three of our galaxies (Fig. 2). An exception is *HZ6*, which is a gravitationally interacting three-component major merger and can be fit with optically thick emission below 200 μm ($\lambda_0 = 200$ μm).

(iv) The molecular gas masses range between 10^{10} and 10^{11} $M_\odot$, corresponding to molecular gas fractions between 30 and 80 per cent (Fig. 5). They are in good agreement with the difference between dynamical and stellar masses. From this, we expect gas depletion time scales of 100–220 Myr in good agreement with the expected decrease of depletion time with redshift. A comparison to gas masses derived from CO($2-1$) emission suggests an $\alpha_{\rm CO}$ conversion factor for *HZ6* and *HZ10* similar to our Milky Way (high values as measured in the SMC can be excluded).

At $z < 4$, several studies find an increase in dust peak temperature (meaning the wavelength at which the IR SED peaks) at a roughly fixed total IR luminosity. Our sample and measurements at $z > 6$ do not suggest a further increase of temperature beyond $z = 5$. The generally higher peak temperatures at $z = 5.5$ compared to average local galaxies can be explained by the decreasing dust abundance (or density) at high redshifts. Specifically, as the dust opacity drops, hot dust becomes more optically thin and is visible to the external observer. This could be related to a lower metallicity as suggested by metal-poor local dwarf galaxies which show an increase temperature compared to other local galaxies of higher metallicity. The lack of dust temperature evolution at $z > 5$ can be explained in similar terms. Our model shows that once the dust density falls below a certain value, the emergent peak temperature ceases to rise. Interestingly, this limit is on the same order of magnitude as the average dust mass density expected for our galaxies.

Compared to DSFGs at similar redshifts ($z > 5$), our galaxies have warmer temperatures than what would be expected from their (factor of 10) lower IR luminosities. This difference could be explained by a larger dust abundance and/or higher metal content of DSFGs and is in agreement with our model predictions. Metallicity measurements with the *James Webb Space Telescope* for these two populations of galaxies will certainly help to identify what causes these differences.

One of the remaining interesting questions is the connection between dust and gas. While a decrease of dust abundance or dust density may explain the observed $T_{\rm peak} - z$ evolution, at the same time the observed increase of the gas fraction (and hence dust abundance given a fixed gas-to-dust ratio) with redshift would argue for the opposite. An increasing gas-to-dust ratio with redshift due to a general decrease in metallicity (e.g. Leroy et al. 2011) could resolve this dilemma.

The number of ALMA observations at high redshifts is increasing rapidly as large surveys are becoming more frequent. Our Band 8 data are an important step to constrain better the IR SEDs of post-reionization galaxies. They can be used to inform and improve the assumptions that have to be made in order to measure important IR SED based quantities as well as to test theoretical predictions. However, our conclusions are currently based on a sample of only four galaxies, which are, due to observing time constraints, among the IR brightest galaxies at $z \sim 5.5$. Larger samples with similar measurements are crucial to advance our understanding. As shown

by the comparison of gas masses derived by the dust-continuum and the CO(2 − 1) emission, at least *HZ6* and *HZ10* have similar CO to H_2 conversion factors to our Milky Way, which suggests metal-enriched environments. This is also suggested by the deep absorption features of their rest-frame UV spectra. It is therefore likely that we are missing more metal-poor systems, which could be the more common type of galaxies. Furthermore, our small sample also shows a diversity of galaxies (isolated galaxies, mergers, etc.) that links to different dust properties, which should be explored. Our simple model can motivate certain trends seen in our sample, but to understand in depth the physics driving the observational results, similar observations for larger samples will be necessary in the future.

ACKNOWLEDGEMENTS

This paper makes use of the following ALMA data: ADS/JAO.ALMA#2018.1.00348.S, ADS/JAO.ALMA#2017.1.00428.L, ADS/JAO.ALMA#2015.1.00388.S, ADS/JAO.ALMA#2015.1.00928.S, ADS/JAO.ALMA#2012.1.00523.S. ALMA is a partnership of ESO (representing its member states), NSF (USA) and NINS (Japan), together with NRC (Canada), MOST and ASIAA (Taiwan), and KASI (Republic of Korea), in cooperation with the Republic of Chile. The Joint ALMA Observatory is operated by ESO, AUI/NRAO and NAOJ. The National Radio Astronomy Observatory is a facility of the National Science Foundation operated under cooperative agreement by Associated Universities, Inc. This work was supported by the Swiss National Science Foundation through the SNSF Professorship grant 157567 'Galaxy Build-up at Cosmic Dawn'. DAR acknowledges support from the National Science Foundation under grant numbers AST-1614213 and AST-1910107. DAR also acknowledges support from the Alexander von Humboldt Foundation through a Humboldt Research Fellowship for Experienced Researchers. Finally, we thank the referee for the very useful comments that improved this manuscript.

DATA AVAILABILITY

The data underlying this paper were accessed from the ALMA science archive (http://almascience.nrao.edu/aq/). The program identifiers are ADS/JAO.ALMA#2018.1.00348.S, ADS/JAO.ALMA#2017.1.00428.L, ADS/JAO.ALMA#2015.1.00388.S, ADS/JAO.ALMA#2015.1.00928.S, and ADS/JAO.ALMA#2012.1.00523.S. The individual and stacked best-fitting IR SEDs (Fig. 3) are available in the online version or on request.

REFERENCES

Ando M., Ohta K., Iwata I., Akiyama M., Aoki K., Tamura N., 2007, PASJ, 59, 717
Arnouts S., Cristiani S., Moscardini L., Matarrese S., Lucchin F., Fontana A., Giallongo E., 1999, MNRAS, 310, 540
Bakx T. J. L. C. et al., 2020, MNRAS, 493, 4294
Barnabè M. et al., 2012, MNRAS, 423, 1073
Béthermin M. et al., 2015, A&A, 573, A113
Bethermin M. et al., 2020, preprint (arXiv:2002.00962)
Blain A. W., Barnard V. E., Chapman S. C., 2003, MNRAS, 338, 733
Bouché N. et al., 2012, MNRAS, 419, 2
Bouwens R. J. et al., 2009, ApJ, 705, 936
Bouwens R. J. et al., 2012, ApJ, 754, 83
Bouwens R. J. et al., 2014, ApJ, 793, 115
Calzetti D., 2001, PASP, 113, 1449
Capak P. L. et al., 2011, Nature, 470, 233
Capak P. L. et al., 2015, Nature, 522, 455
Casey C. M., 2012, MNRAS, 425, 3094
Chabrier G., 2003, PASP, 115, 763
Conley A. et al., 2011, ApJ, 732, L35
D'Odorico V. et al., 2018, ApJ, 863, L29
da Cunha E. et al., 2015, ApJ, 806, 110
Davidzon I. et al., 2017, A&A, 605, A70
Davidzon I., Ilbert O., Faisst A. L., Sparre M., Capak P. L., 2018, ApJ, 852, 107
de Barros S., Schaerer D., Stark D. P., 2014, A&A, 563, A81
De Looze I. et al., 2014, A&A, 568, A62
Dessauges-Zavadsky M. et al., 2020, preprint (arXiv:2004.10771)
Draine B. T., 2006, ApJ, 636, 1114
Dudzevičiūtė U. et al., 2020, MNRAS, 494, 3828
Faisst A. L., 2016, ApJ, 829, 99
Faisst A. L. et al., 2016a, ApJ, 821, 122
Faisst A. L. et al., 2016b, ApJ, 822, 29
Faisst A. L. et al., 2017, ApJ, 847, 21
Faisst A. et al. 2019, preprint (arXiv:1901.01268)
Faisst A. L. et al., 2020, ApJS, 247, 61
Ferrara A., Hirashita H., Ouchi M., Fujimoto S., 2017, MNRAS, 471, 5018
Finkelstein S. L. et al., 2012, ApJ, 756, 164
Freundlich J. et al., 2019, A&A, 622, A105
Fudamoto Y. et al., 2017, MNRAS, 472, 483
Fudamoto Y. et al., 2020, preprint (arXiv:2004.10760)
Genzel R. et al., 2015, ApJ, 800, 20
Harikane Y. et al., 2019, ApJ, 896, 19
Hashimoto T. et al., 2019, PASJ, 71, 71
Hasinger G. et al., 2018, ApJ, 858, 17
Hildebrand R. H., 1983, QJRAS, 24, 267
Hoffman M. D., Gelman A., 2011, preprint (arXiv:1111.4246)
Hughes T. M. et al., 2017, MNRAS, 468, L103
Ilbert O. et al., 2006, A&A, 457, 841
Issa M. R., MacLaren I., Wolfendale A. W., 1990, A&A, 236, 237
Kaasinen M. et al., 2019, ApJ, 880, 15
Kennicutt R. C., Jr, 1998, ARA&A, 36, 189
Kennicutt R. C. et al., 2011, PASP, 123, 1347
Khusanova Y. et al., 2020, A&A, 634, A97
Knudsen K. K., Richard J., Kneib J.-P., Jauzac M., Clément B., Drouart G., Egami E., Lindroos L., 2016, MNRAS, 462, L6
Labbé I. et al., 2013, ApJ, 777, L19
Le Fèvre O., Béthermin M., Faisst A., Capak P., Cassata P., Silverman J. D., Schaerer D., Yan L., 2019, preprint (arXiv:1910.09517)
Leroy A. K. et al., 2011, ApJ, 737, 12
Liang L. et al., 2019, MNRAS, 489, 1397
Lilly S. J., Carollo C. M., Pipino A., Renzini A., Peng Y., 2013, ApJ, 772, 119
Lisenfeld U., Ferrara A., 1998, ApJ, 496, 145
Lu N. et al., 2018, ApJ, 864, 38
Ma X. et al., 2019, MNRAS, 487, 1844
Madden S. C. et al., 2013, PASP, 125, 600
Magdis G. E. et al., 2012, ApJ, 760, 6
Magnelli B. et al., 2014, A&A, 561, A86
Mannucci F., Cresci G., Maiolino R., Marconi A., Gnerucci A., 2010, MNRAS, 408, 2115
Meurer G. R., Heckman T. M., Calzetti D., 1999, ApJ, 521, 64
Misselt K. A., Clayton G. C., Gordon K. D., 1999, ApJ, 515, 128
Nakajima K., Ouchi M., 2014, MNRAS, 442, 900
Neal R. M., 2012, preprint (arXiv:1206.1901)
Oke J. B., 1974, ApJS, 27, 21
Pak S., Jaffe D. T., van Dishoeck E. F., Johansson L. E. B., Booth R. S., 1998, ApJ, 498, 735
Pavesi R. et al., 2018a, ApJ, 861, 43
Pavesi R. et al., 2018b, ApJ, 864, 49

Pavesi R., Riechers D. A., Faisst A. L., Stacey G. J., Capak P. L., 2019, ApJ, 882, 168
Prevot M. L., Lequeux J., Prevot L., Maurice E., Rocca-Volmerange B., 1984, A&A, 132, 389
Rangwala N. et al., 2011, ApJ, 743, 94
Riechers D. A. et al., 2013, Nature, 496, 329
Riechers D. A. et al., 2014, ApJ, 796, 84
Riechers D. A. et al., 2019, ApJ, 872, 7
Riechers D. A. et al., 2020, ApJ, 895, 28
Schreiber C. et al., 2018, A&A, 618, A85
Scoville N. Z., Kwan J., 1976, ApJ, 206, 718
Scoville N. et al., 2007, ApJS, 172, 1
Scoville N. et al., 2014, ApJ, 783, 84
Scoville N. et al., 2016, ApJ, 820, 83
Scoville N. et al., 2017, ApJ, 837, 150
Simpson J. M. et al., 2017, ApJ, 839, 58
Skibba R. A. et al., 2011, ApJ, 738, 89
Sommovigo L., Ferrara A., Pallottini A., Carniani S., Gallerani S., Decataldo D., 2020, MNRAS, 496, 956
Tacconi L. J. et al., 2010, Nature, 463, 781
Walter F. et al., 2012, ApJ, 752, 93
Willott C. J., Carilli C. L., Wagg J., Wang R., 2015, ApJ, 807, 180
Zanella A. et al., 2018, MNRAS, 481, 1976

SUPPORTING INFORMATION

Supplementary data are available at *MNRAS* online.

data.zip

Please note: Oxford University Press is not responsible for the content or functionality of any supporting materials supplied by the authors. Any queries (other than missing material) should be directed to the corresponding author for the article.

APPENDIX: DIFFERENT WAYS TO FIT IR SEDS

To fit the IR SEDs of our galaxies, we have assumed a modified blackbody parametrization including a mid-IR power law as described in Casey (2012) and Blain et al. (2003). Here, we compare this approach to different parametrizations.

First, the mid-IR power-law slope α (which we fix at 2) is not constrained by our observations. This slope may range between values of 0.5 and 5.5 depending on the amount of mid-IR emission Casey (2012). We find that changing α within that range alters the temperatures by less than 5 K. As a second test, we entirely removed the mid-IR dependence and fit only the first term of equation (1) (while fixing $\lambda_0 = 100\,\mu$m). The resulting peak temperatures are 41.0, 30.5, 38.6, and 35.4 K and emissivities (β_d) of 2.2, 1.7, 2.1, and 2.3 for *HZ4*, *HZ6*, *HZ9*, and *HZ10*, respectively. The peak temperatures are within 3 K of the ones reported with $\alpha = 2$ and also the emissivities are very consistent within 0.2 (cf. Table 3). We therefore conclude that the (unknown) mid-IR power-law slope does not impact our measurements significantly.

Secondly, we investigated the case of a modified blackbody without mid-IR power law in the optically thin limit. In this case, we fit the IR SEDs using

$$S(\lambda) = N_{\rm bb} \times \frac{\lambda^{-(3+\beta)}}{e^{(h\,c)/(\lambda\,k\,\hat{T}_{\rm SED})} - 1}. \quad \text{(A1)}$$

From this, we get peak temperatures of 96.0, 30.5, 47.5, and 45.1 K and emissivities (β_d) of 1.6, 1.9, 1.7, and 1.8 for *HZ4*, *HZ6*, *HZ9*, and *HZ10*, respectively (see Fig. A1). The change for *HZ4* is the largest, which we trace back to its faintness, making its uncertainty large. The estimated 1σ probability envelope covers temperatures between 55 and 130 K. For *HZ6*, we do not find a significant different. On the other hand, the peak temperatures of *HZ9* and *HZ10* are increased by 8.6 and 7.7 K, respectively. As we are using here the optically thin limit, these temperatures provide an absolute upper limit for these galaxies. The true temperatures lies likely between the optically thin limit and $\lambda_0 = 100\,\mu$m, which would put these temperatures still consistently below the temperature predicted at $z = 5.5$ from the extrapolation of the Schreiber et al. (2018) data (see Section 4).

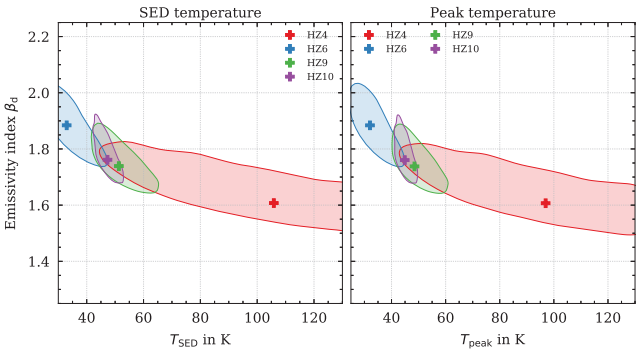

Figure A1. Same as Fig. 4, but for a modified blackbody model without mid-IR power law in the case of the optically thin limit (see equation A1).

This paper has been typeset from a TEX/LATEX file prepared by the author.